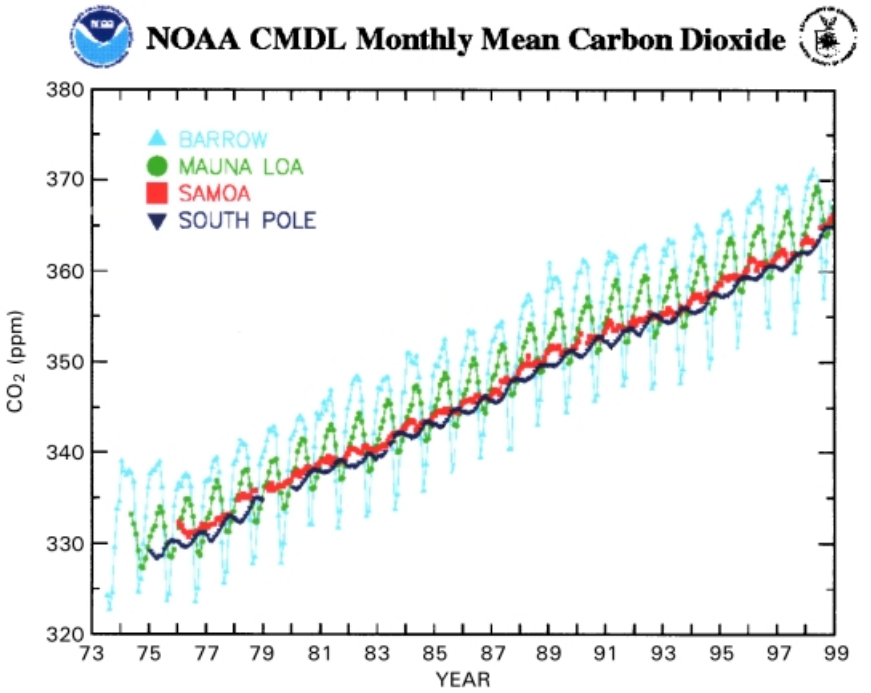

Atmospheric carbon dioxide mixing ratios determined from the continuous monitoring programs at the 4 NOAA CMDL baseline observatories. Principal investigator: Pieter Tans, NOAA CMDL Carbon Cycle Group, Boulder, Colorado, (303) 497-6678. ptans@cmdl.noaa.gov.

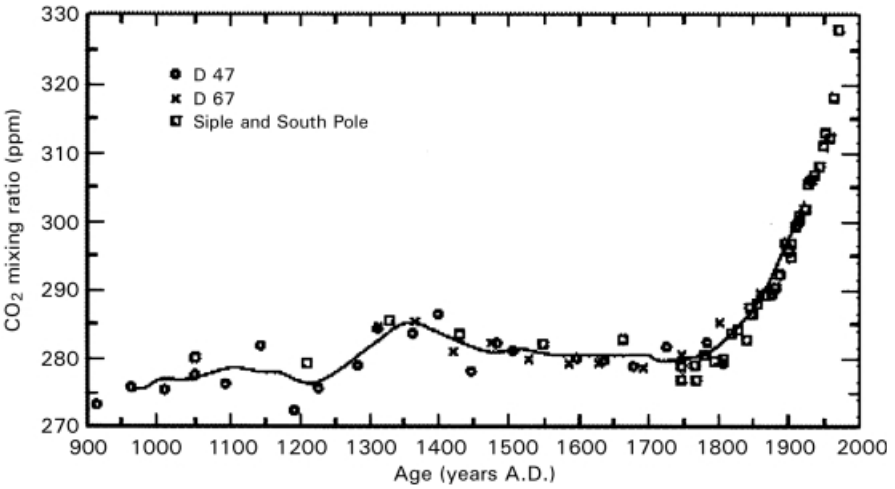

Figure 5 (Chapter 1) (*a*) Monthly concentrations of CO_2 measured from gas samples at four monitoring sites operated by NOAA's Climate Monitoring and Diagnostics Laboratory from the early 1970s; (*b*) CO_2 concentrations determined from ice core samples estimated to go back ~1000 years.

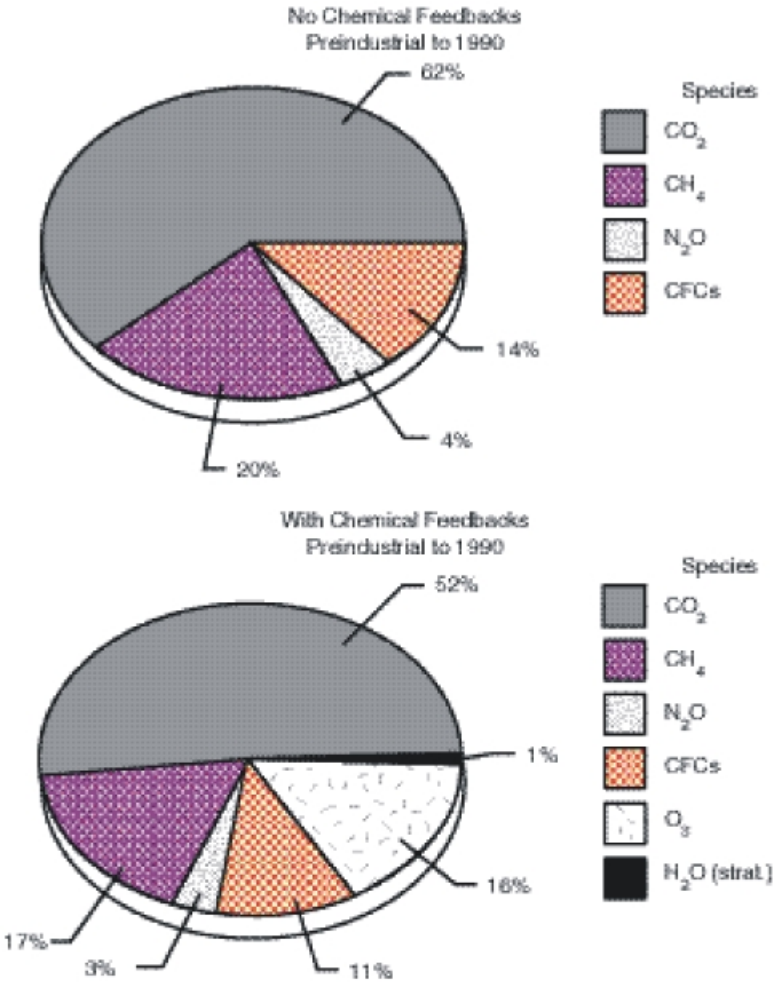

Figure 8 (Chapter 1) Contributions of various trace gases to global warming. Top graph shows the calculations using a model that does not include contributions from tropospheric ozone increases or from feedback relating to photochemical processes; bottom chart shows contributions using a model that includes photochemical feedback mechanisms.

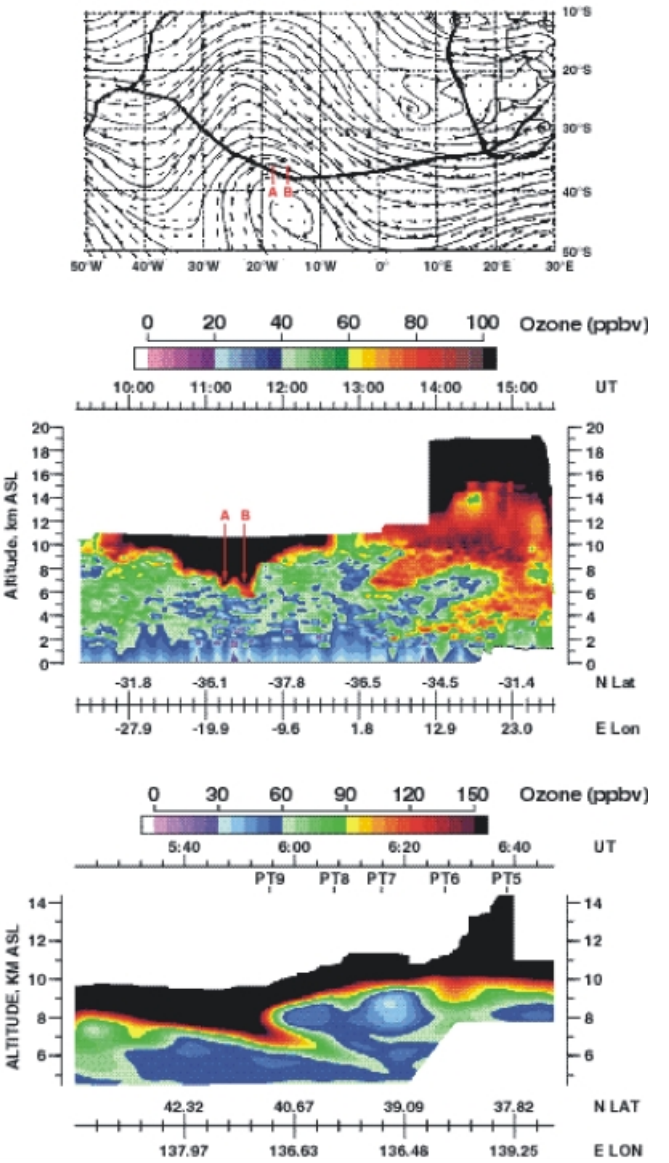

Figure 10 (Chapter 1) Three-panel figure showing evidence of ozone input from the stratosphere into the troposphere in both hemispheres. The top panel shows the flight path (heavy line) of a DC-8 airplane on October 3, 1992, from South America to Africa that intersected a trough protruding from higher latitudes. Points A and B on that flight path show high concentrations of ozone being transported to altitudes below 6 km in the middle panel; the data depicted in this panel were obtained from a differential absorption lidar system that measured ozone below the 11-km flight level of the DC-8. The lowest panel shows a similar feature for a flight on March 11, 1994, in the Northern Hemisphere. As the airplane flies from north to south in this panel, note the higher tropopause height south of the fold.

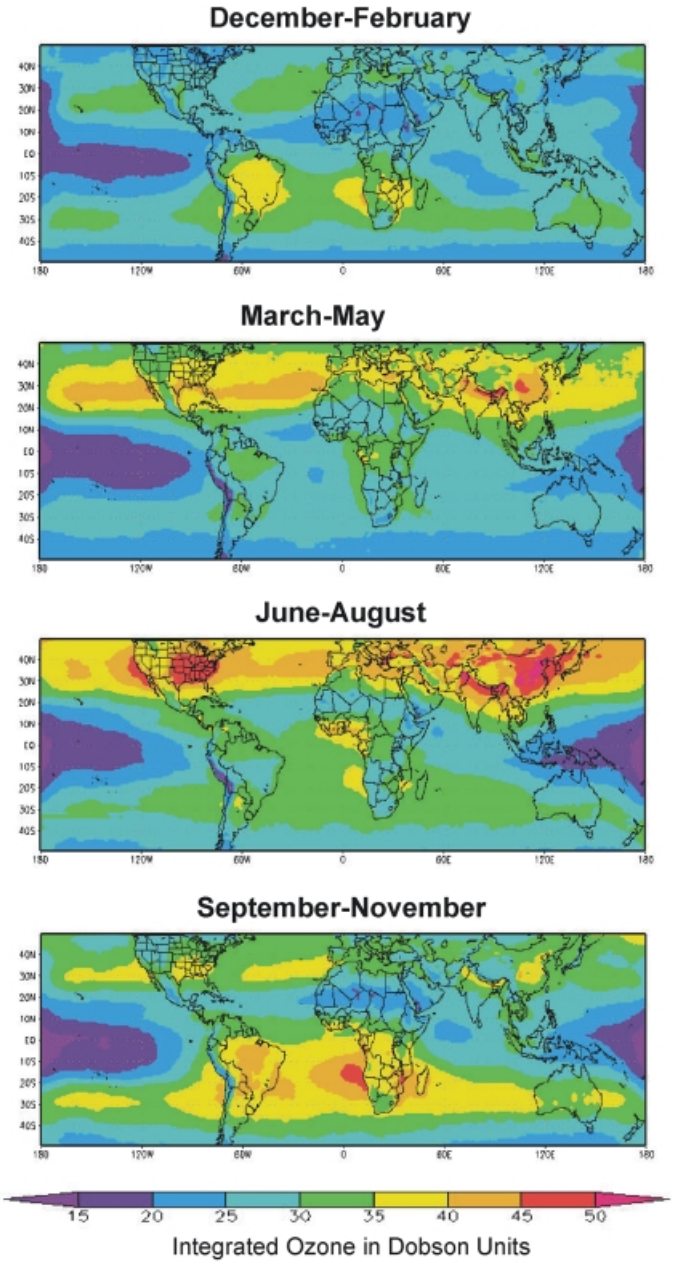

Figure 1 (Chapter 3) Climatological distribution of tropospheric ozone derived from satellite measurements between 1979 and 2000 (from Fishman et al., 2002). Units of contours and Dobson Units (DU). Regions greater than 40 DU have been shaded.

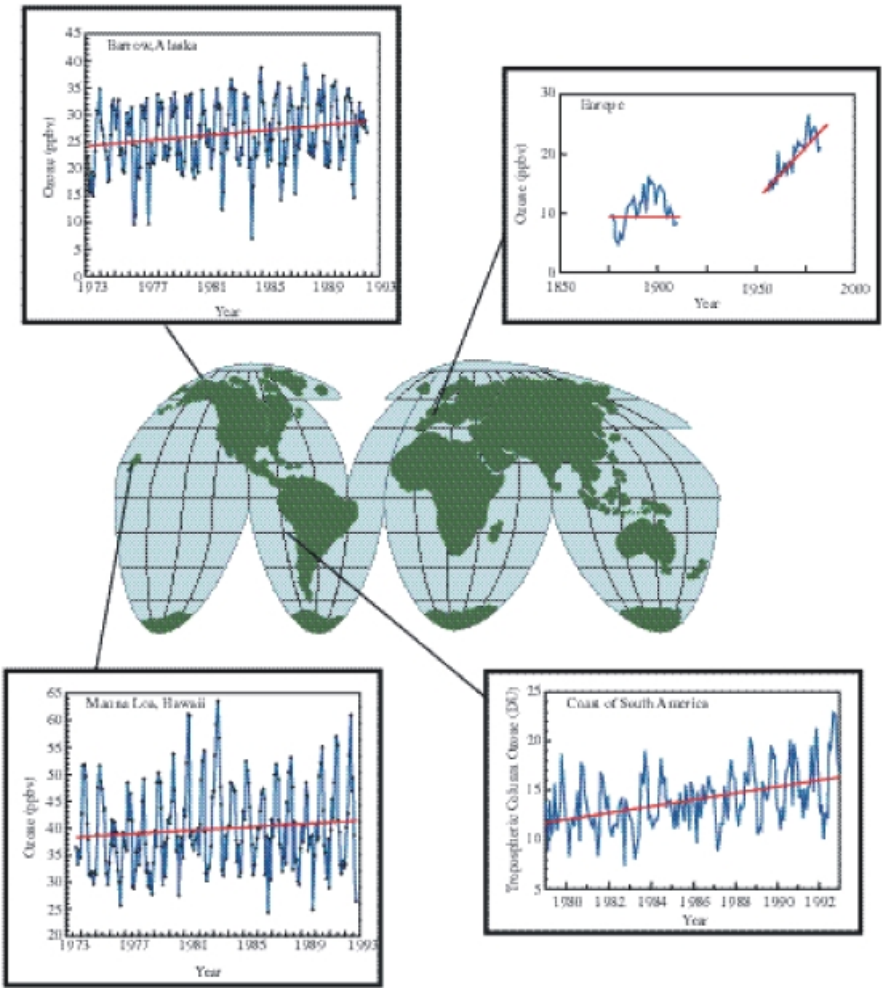

Figure 2 (Chapter 3) (*a*) (Upper left): monthly mean surface ozone at Barrow and the linear trend for the entire data record. (Lower left): monthly mean surface ozone at Mauna Loa with the linear trend. (Upper right) annual mean ozone concentrations at Montsouris Observatory outside Paris (1876–1910) and Arkona, East Germany (1956–1984). The average ozone concentration at the beginning of the twentieth century near Paris was less than 10 ppb whereas in 1985 the typical ground-level concentrations in central Europe is approaching 30 ppb, implying an increase of about 200% during the century (from Volz and Kley, 1988). (Lower right): ozone trend off coast of South America determined from analysis of satellite measurements of total ozone (from Jiang and Yung, 1996).

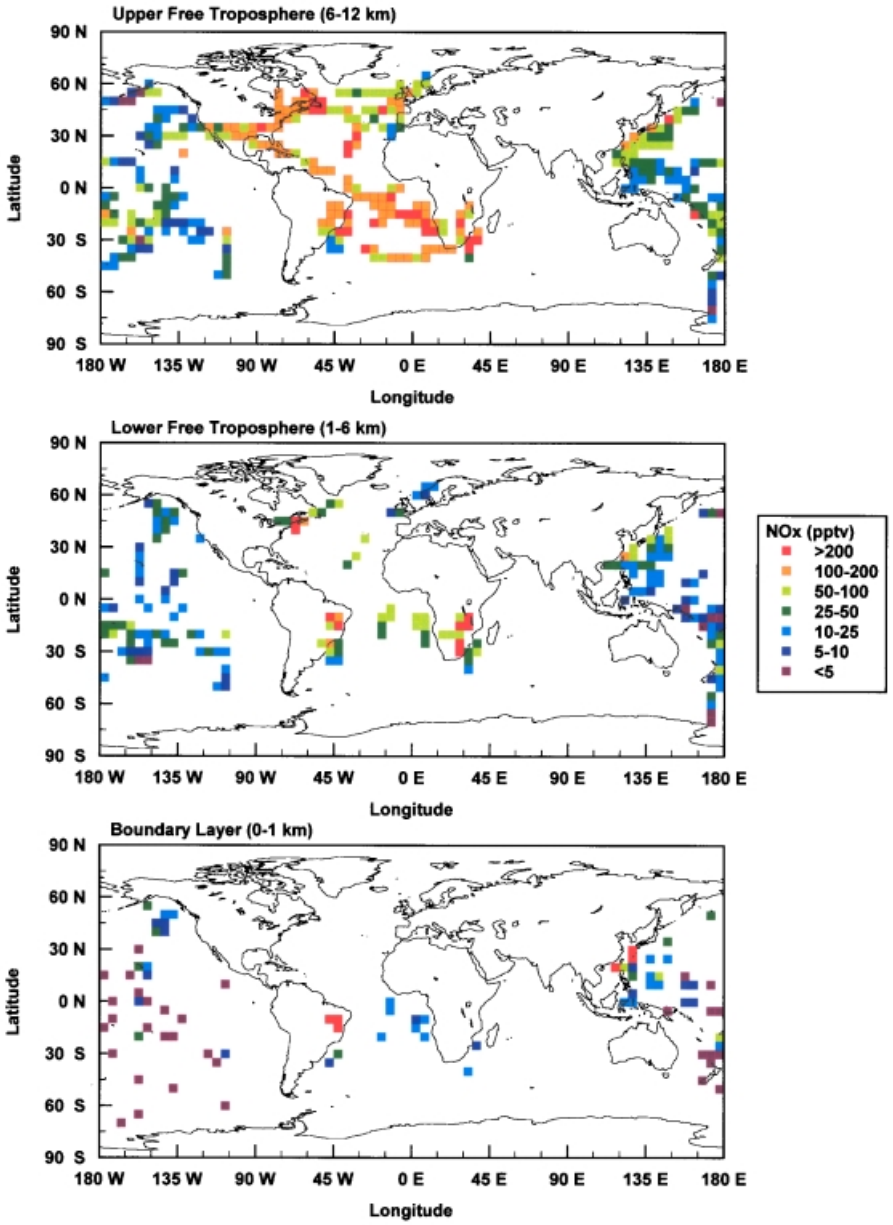

Figure 3 (Chapter 4) Distribution of NO_x based on measurements taken from NASA's DC-8 aircraft during fall (see text for details). Data are averaged on a $5^\circ \times 5^\circ$ latitude–longitude grid for three altitude ranges.

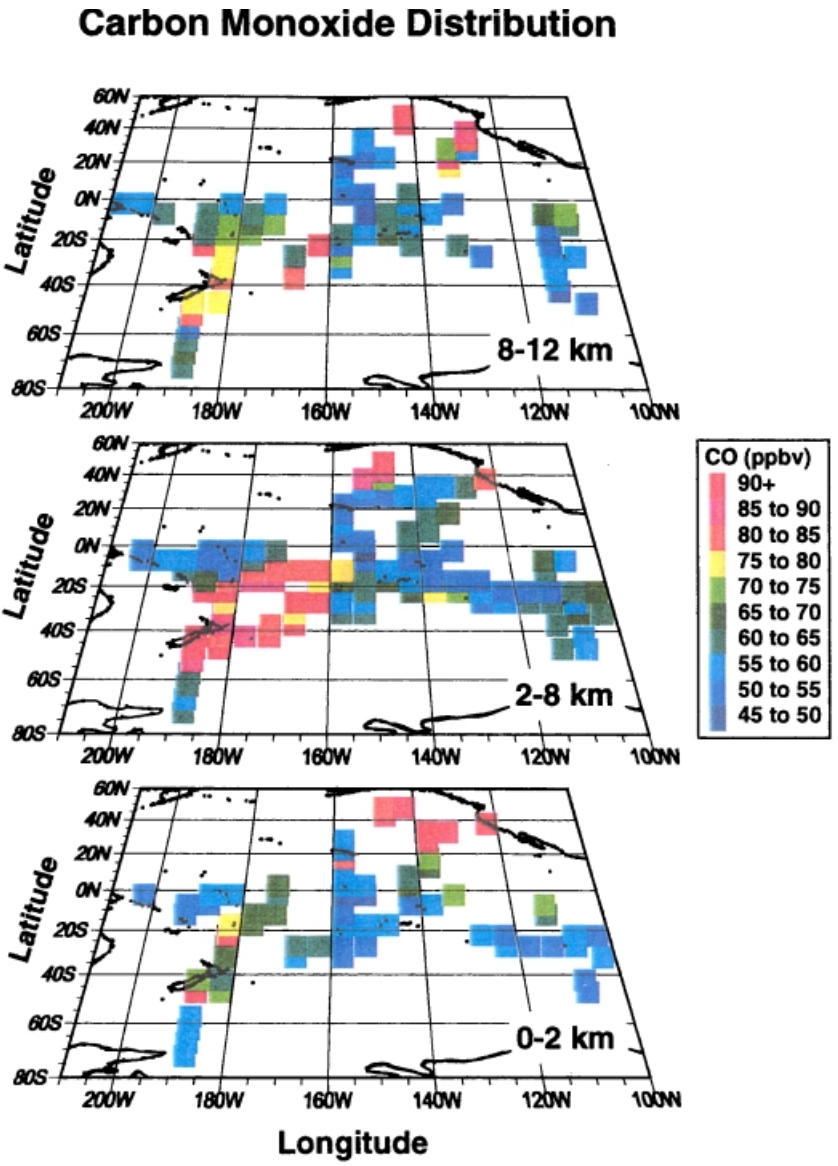

Figure 4 (Chapter 14) CO over tropical Pacific during September 1996 PEM–Tropics A sampling (from Blake et al., 1999). Measurements by G. W. Sachse with a lidar-based instrument. Analysis of possible fire sources is described by Olson et al. (1999).

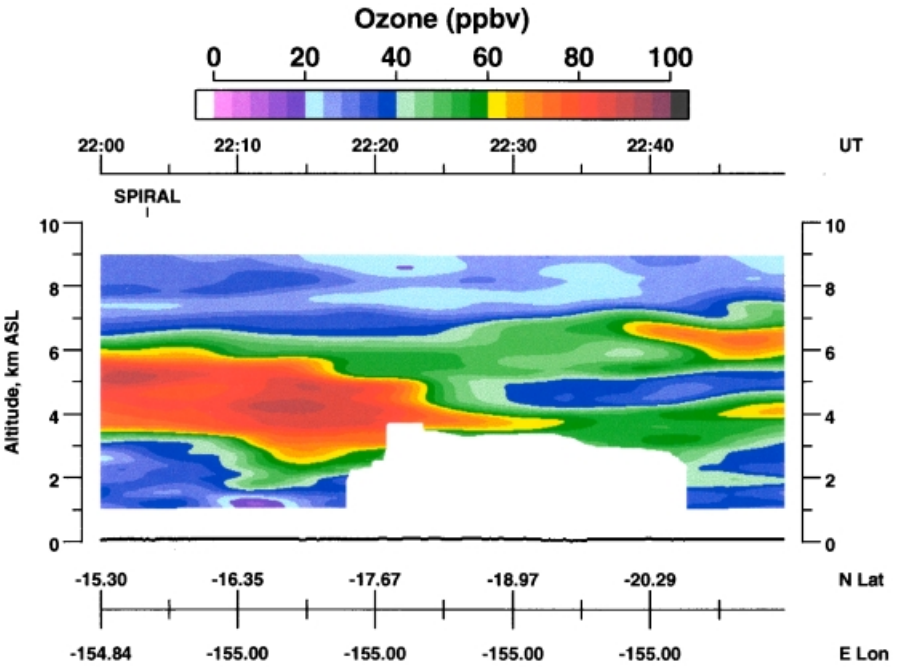

Figure 5 (Chapter 14) Ozone plume over the Pacific seen during the PEM–Tropics A aircraft mission in Sept.–Oct. 1996. (from Fenn et al., 1999).

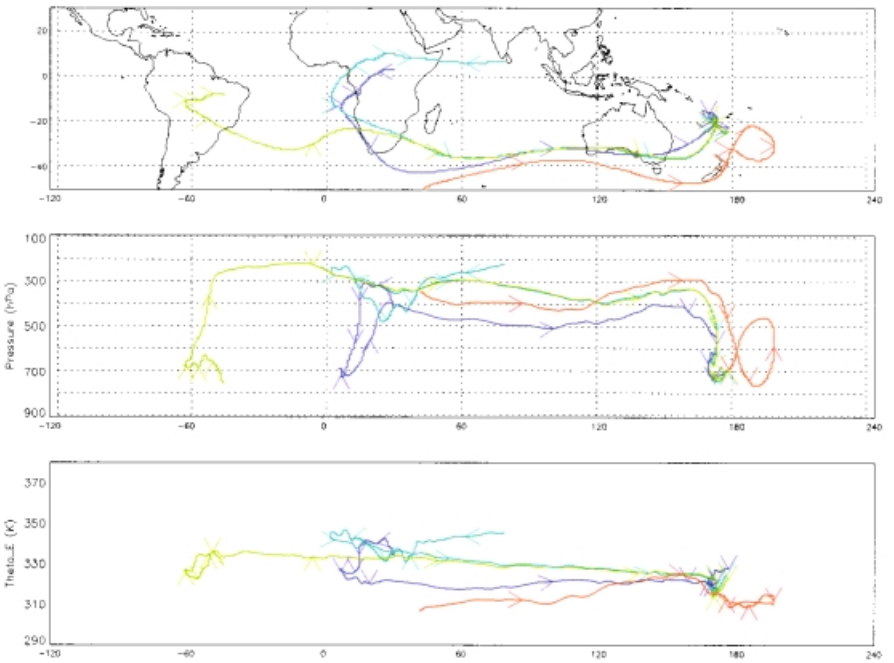

Figure 6 (Chapter 14) (*b*) Aspects of the "Southern Global Plume" from Guo and Chatfield (1998). Back trajectories are initiated at several points along the NASA DC-8 flight of September 23–24, 1996 (PEM–Tropics A). Top panel shows traces back to origin areas in South America and Africa. Middle panel shows pressures of trajectories. Directional arrows are spaced every 2 days. Lowest panel shows potential temperature of trajectory, which is nearly conserved, demonstrating that trajectory does not cross into other air masses. Model is based on MM5 mesoscale model.

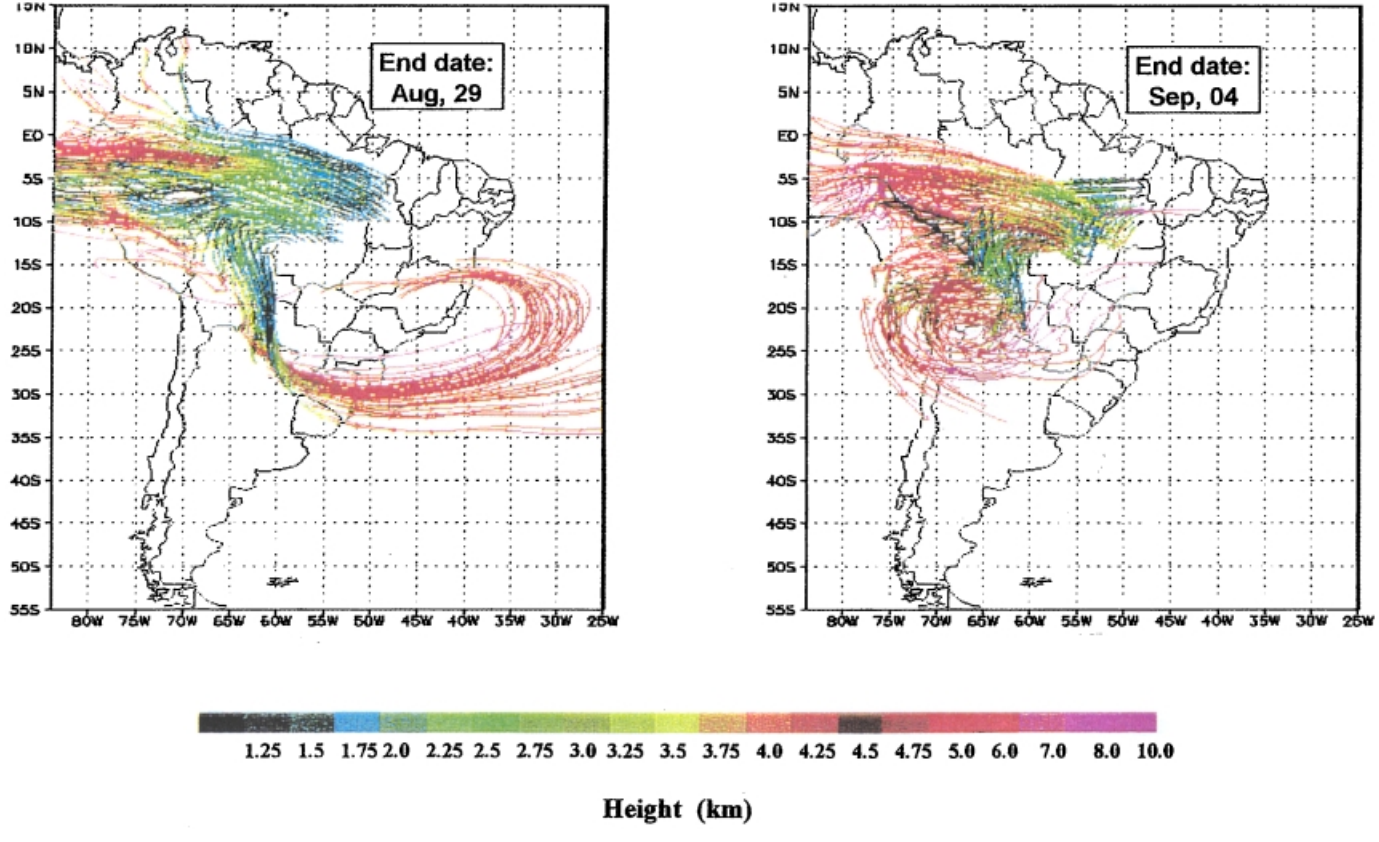

Figure 8 (Chapter 14) Composite of forward trajectories from Cuiabá during the 1995 SCAR-B field experiment. A Brazilian version of the Colorado State mesoscale RAMS model was used to provide winds for the University of São Paulo kinematic trajectory model (from Longo et al., 1999).

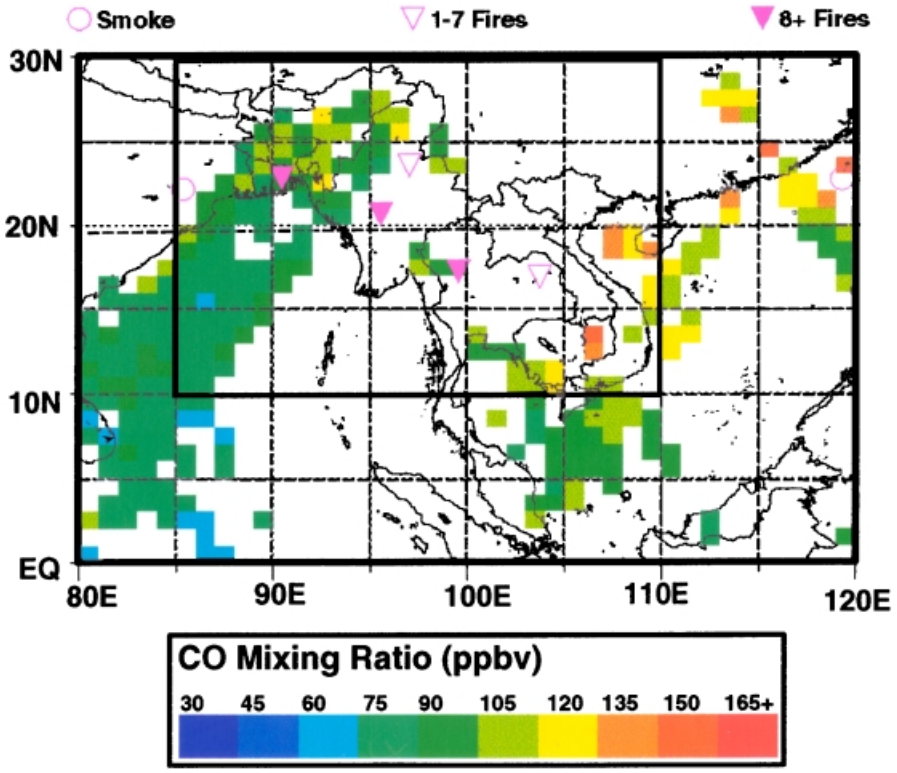

Figure 10 (Chapter 14) (*a*) MAPS CO, April 1994 (from Christopher et al., 1998).

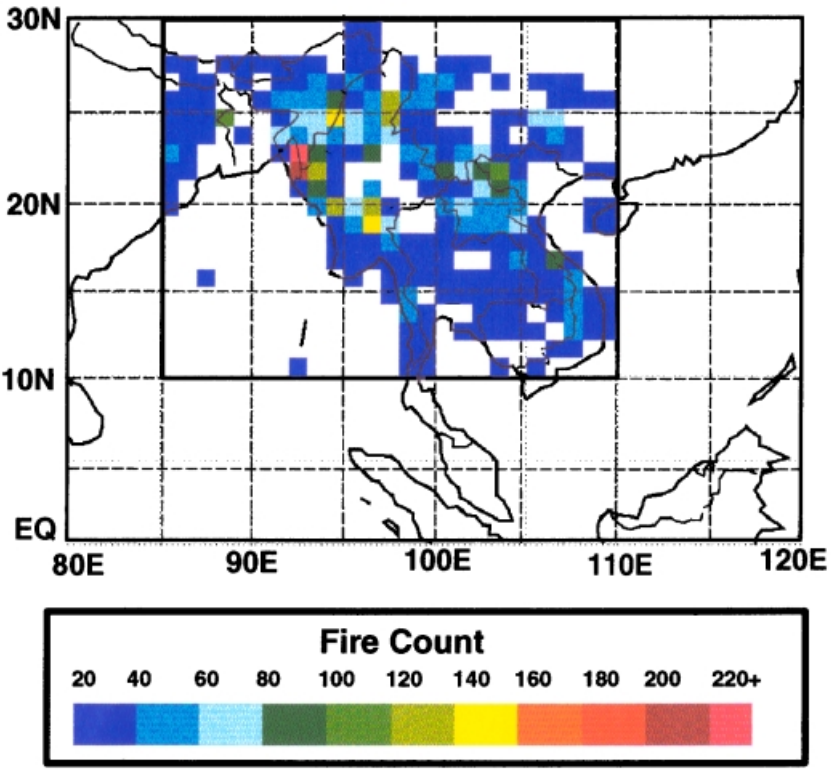

Figure 10 (Chapter 14) (*b*) coincident fires during April 1994 Space Shuttle flight (from Christopher et al., 1998).

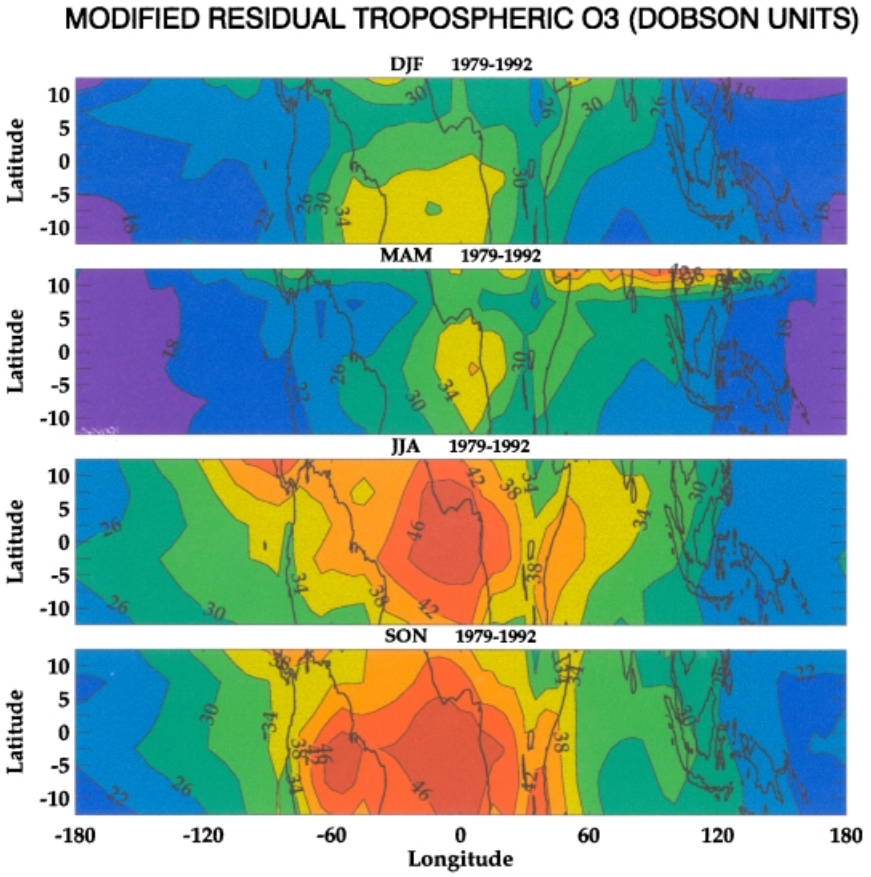

Figure 12 (Chapter 14) Wave-one pattern in tropospheric ozone apparent in TOMS satellite data, averaged from 2 maps/month during the 1979–1992 *Nimbus 7* observing period. Wave appears to be present throughout year. Scale is DU (Dobson units). Cf. Figure A1 in Thompson and Hudson (1999).

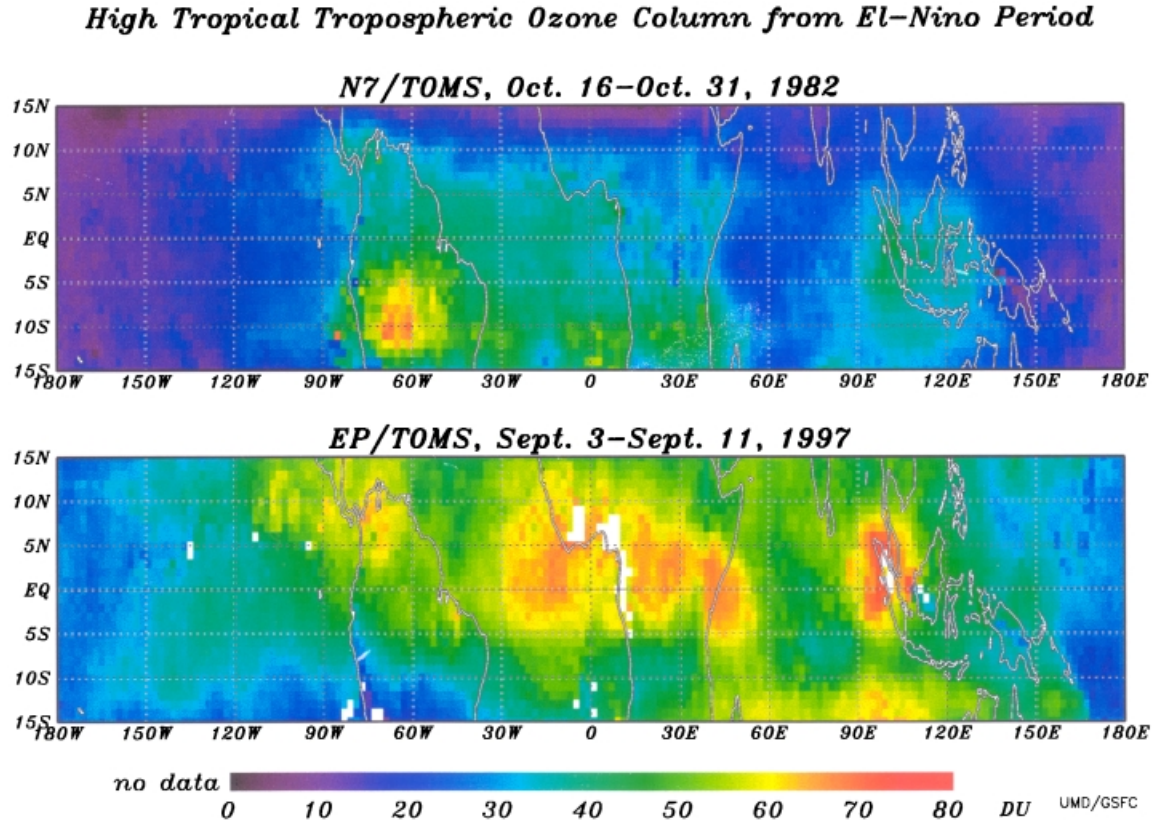

Figure 14 (Chapter 14) Tropospheric column ozone (in DU, from modified-residual method; Thompson and Hudson, 1999) during El Niño-Southern Oscillation (ENSO) of late 1982 (upper panel) as seen in tropical tropospheric ozone map and for September 1997 (lower panel).

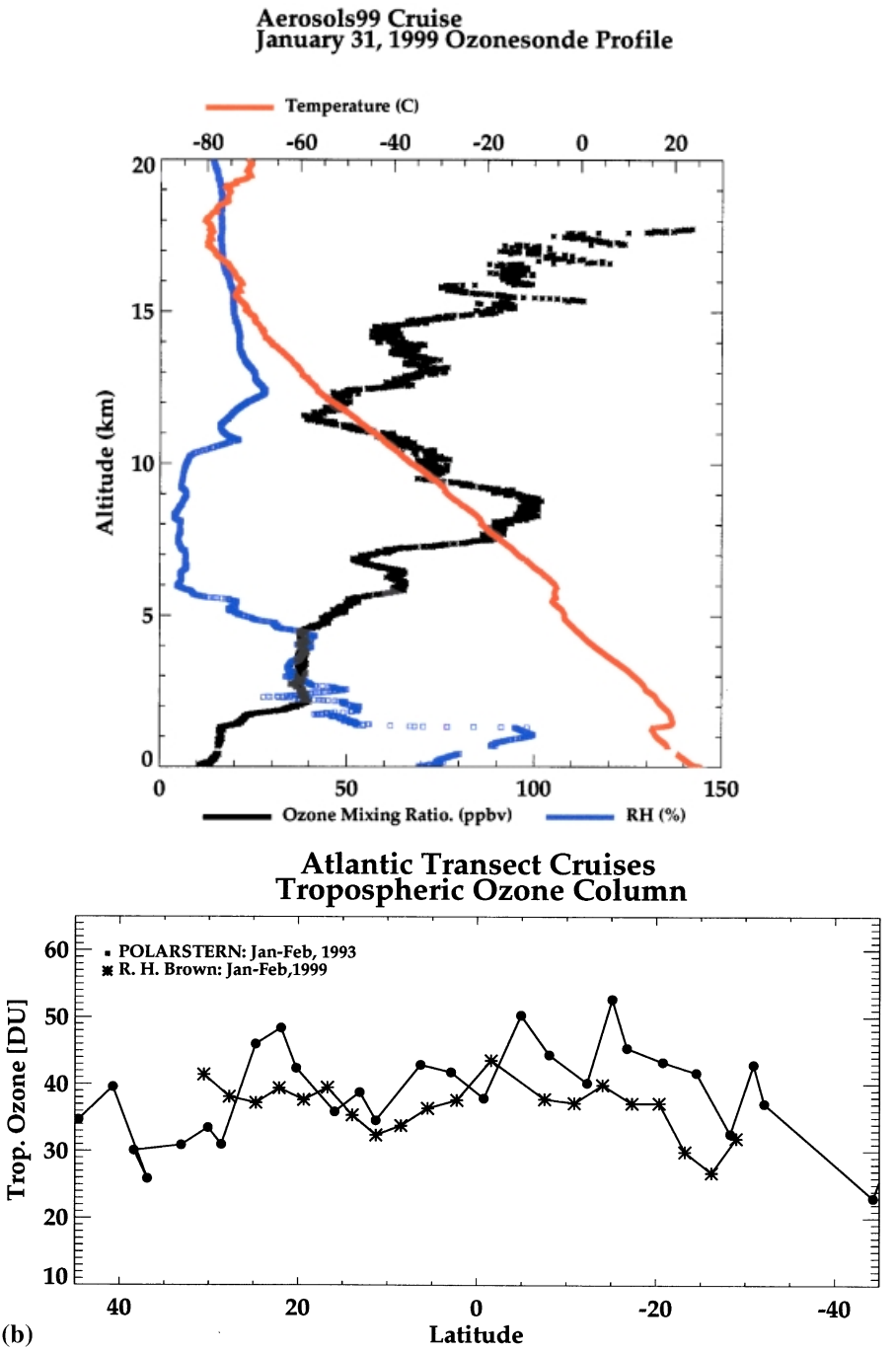

Figure 15 (Chapter 14) (*a*) Profiles of ozone, temperature and water vapor (as percent relative humidity) from 0 to 20 km on January 31, 1999 during Aerosols99 cruise of R/V *Ronald H. Brown*. Anti-correlation of high ozone between 7 and 10 km suggestive of aged stratospheric air. (*b*) Comparison of integrated tropospheric column ozone from sondes launched along Atlantic transect of R/V *Ronald H. Brown* (Thompson et al., 2000) in January–February 1999 and from sondes launched along January–February 1993 Atlantic transect of R/V *Polarstern* (Weller et al., 1996).

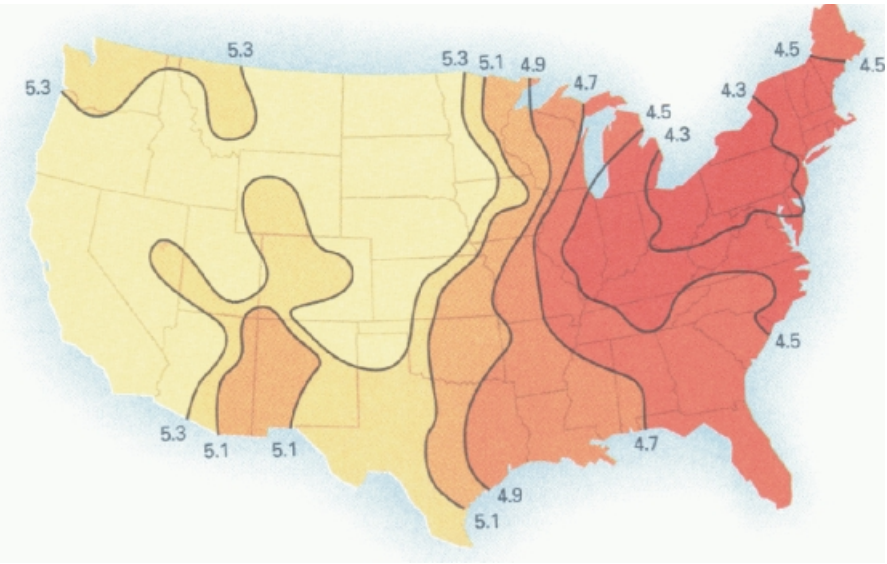

Figure 1 (Chapter 15) Annual pH of rain for the United States in 1990. The black lines indicate contours of equal pH.

Figure 1 (Chapter 16) (*a*) Photographs (*a*) through (*d*) show that, from a visual resource point of view, visibility is not how far a person can see but rather the ability of an observer to clearly see and appreciate the many and varied scenic elements in each vista. (*a*) The farthest scenic feature is the 130-km distant Navajo Mountain, as seen from Bryce Canyon National Park. (*b*) The La Sal Mountains, as seen from the Colorado River, are a dominant view from the distant horizon. (*c*) This view in Canyonlands National Park shows the highly textured foreground canyon walls against the backdrop of the La Sal Mountains. The La Sals are 50 km from the observation point. (*d*) Bryce Canyon as seen from Sunset Point. Notice the highly textured and brightly colored foreground features.

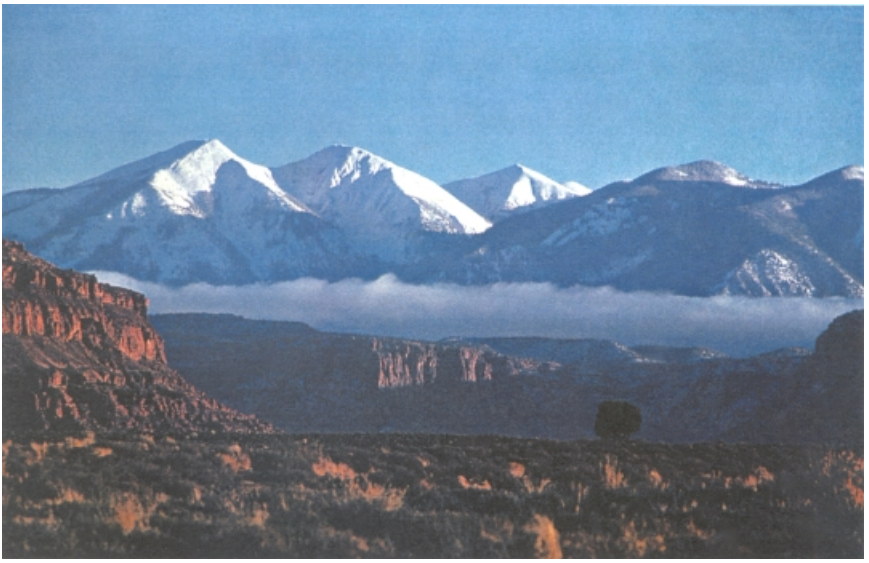

Figure 1 (Chapter 16) (*b*)

Figure 1 (Chapter 16) (*c*)

Figure 1 (Chapter 16) (*d*)

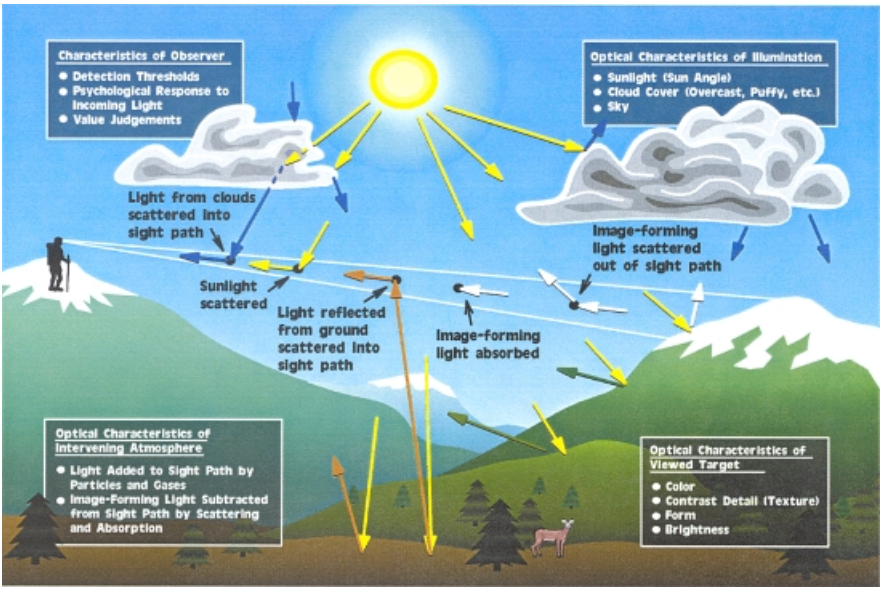

Figure 3 (Chapter 16) Important factors involved in seeing a scenic vista are outlined. Image-forming information from an object is reduced (scattered and absorbed) as it passes through the atmosphere to the human observer. Air light is also added to the sight path by scattering processes. Sunlight, light from clouds, and ground-reflected light all impinge on and scatter from particulates located in the sight path. Some of this scattered light remains in the sight path, and at times it can become so bright that the image essentially disappears. A final important factor in seeing and appreciating a scenic vista are the characteristics of the human observer.

Figure 12 (Chapter 16) (*a*) Effect of regional or uniform haze on a Glacier National Park vista. The view is of the Garden Wall from across Lake McDonald. Atmospheric particulate concentrations associated with photographs (*a*), (*b*), (*c*), and (*d*) correspond to 7.6, 12.0, 21.7, and 65.3 $\mu g/m^3$.

Figure 12 (Chapter 16) (*b*)

Figure 12 (Chapter 16) (*c*)

Figure 12 (Chapter 16) (*d*)

Figure 13 (Chapter 16) Effects of uniform haze on the Chuska Mountains as seen from Mesa Verde National Park. The atmospheric particulate concentration on the day this photograph was taken corresponded to 1 $\mu g/m^3$.

Figure 14 (Chapter 16) Uniform haze degrades visual air quality at Bryce Canyon National Park. The 130-km distant landscape feature is Navajo Mountain. Atmospheric particulate concentration on the day this photograph was taken is 3 $\mu g/m^3$.

Figure 15 (Chapter 16) Navajo Mountain as seen from Bryce Canyon, showing the appearance of layered haze. The pollutants are trapped in a stable air mass that extends from the ground to about half-way up the mountain side.

Figure 16 (Chapter 16) Photograph of Navajo Mountain similar to Figure 15 but with a suspended haze layer that obscures the top portion of the mountain.

Figure 17 (Chapter 16) Classic example of “plume blight.” The thin, dark plume on Navajo Mountain results from a point source emitting particulate matter into a stable atmosphere.

Figure 18 (Chapter 16) Example of one kind of point source that emits pollutants into the atmosphere.

Figure 19 (Chapter 16) Smoke trapped by an inversion layer in the Grand Canyon. During the winter months, inversions are quite common in almost all parts of the United States.

Figure 20 (Chapter 16) Example of power plant emissions trapped in an air inversion layer in the Grand Canyon.

Figure 21 (Chapter 16) Effects of inversion layer in Grand Canyon. In this case, a cloud has formed within the canyon walls.

Figure 22 (Chapter 16) Effects of layered haze trapped in front of the Chuska Mountains as viewed from Mesa Verde National Park. This condition occurs 30 to 40% of the time during winter months.

Figure 23 (Chapter 16) Forest fire plume exemplifying the appearance of carbon particles and demonstrating the effect of lighting. Where the plume is illuminated, it appears gray, but identical particles in the shadow of the plume appear dark or almost black.

Figure 24 (Chapter 16) Example of how light-absorbing particles (in this case carbon) affect the ability to see a vista. Carbon absorbs all wavelengths of light and generally causes a "graying" of the overall scene. Shown here is the north wall of the Grand Canyon as seen from the top of the San Francisco Peaks in northern Arizona.

Figure 25 (Chapter 16) The effect of illumination on the appearance of plumes. The two plumes on the right are identical in terms of their chemical makeup, in that they are primarily water droplets. However, the far right plume is directly illuminated by the sun and the plume second from the right is shaded. The first plume appears white and the second appears almost black. The two plumes on the left are fly-ash plumes.

Figure 26 (Chapter 16) The brown discoloration resulting from an atmosphere containing nitrogen dioxide (NO_2) being shaded by clouds but viewed against a clear blue sky. Light scattered by particulate matter in the atmosphere can cominate light absorbed by NO_2, causing a gray or blue appearing haze (left side of photograph).

Figure 27 (Chapter 16) (*a*) Photographs show how the same haze trapped in an inversion layer looks under forward and backscatter conditions. In (*a*) under forward scattering conditions (morning), the haze appears white; in (*b*) the identical haze, viewed in the afternoon during backscatter conditions, is dark or gray. Because most of the light energy is scattered in the forward direction (white haze), it can be concluded that the particles must be quite large in comparison to the wavelength of light.

Figure 27 (Chapter 16) (*b*)

Figure 28 (Chapter 16) (*a*) Four photographs showing the effect of shifting sun angle on the appearance of a vista as seen from Island in the Sky, Canyonlands National Park. In each photograph, the air quality is the same. In (*a*) (6:00 A.M.) the sun angle–observer–vista geometry results in a large amount of scattered air light (forward scattering) added to the sight path, but minimal amount of imaging light reflected from the vista. Figures 28*b* and 28*c* show a progressively higher sun angle until in Figure 28*d*, the scene is entirely illuminated. Scattered light is minimized and reflected; imaging light is at a maximum.

Figure 28 (Chapter 16) (*b*)

Figure 28 (Chapter 16) (*c*)

Figure 28 (Chapter 16) (*d*)

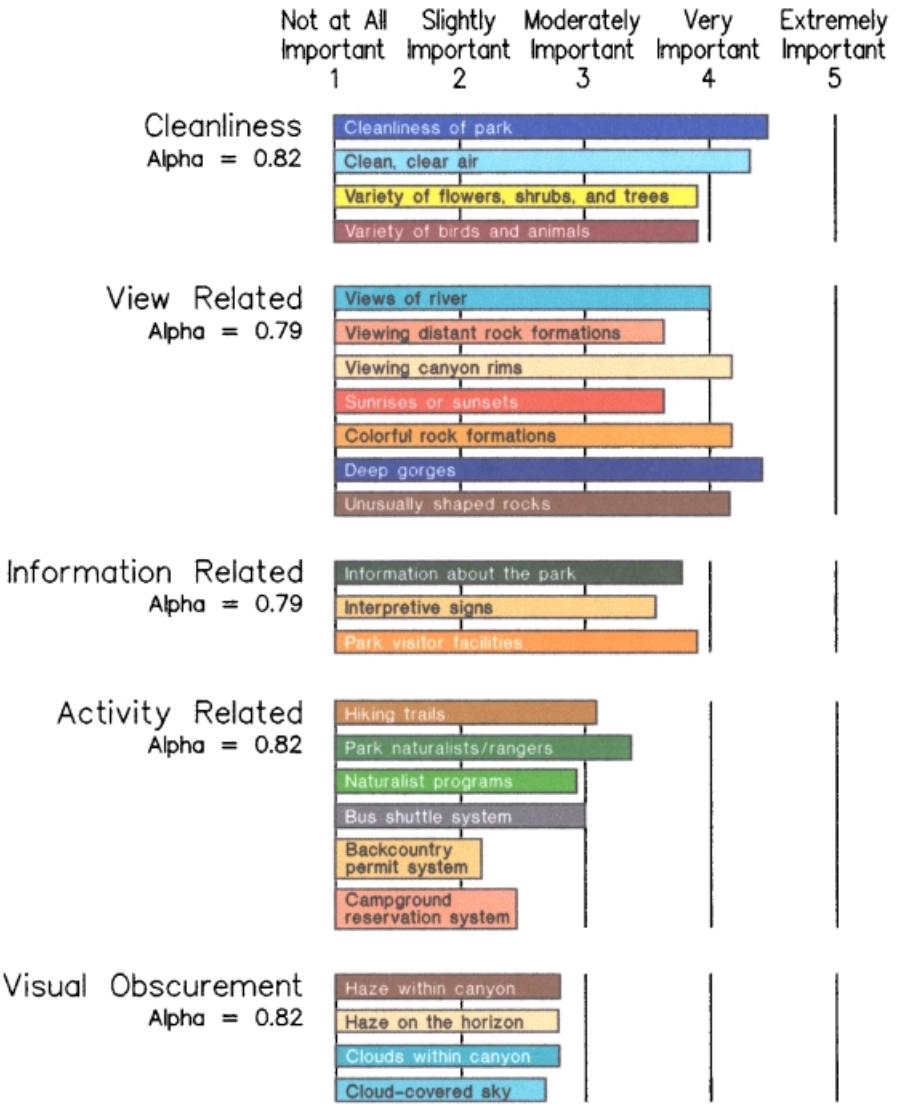

Figure 29 (Chapter 16) Attributes, attribute mean scores, attribute clusters, and attribute cluster mean scores for the Grand Canyon National Park visitor survey.

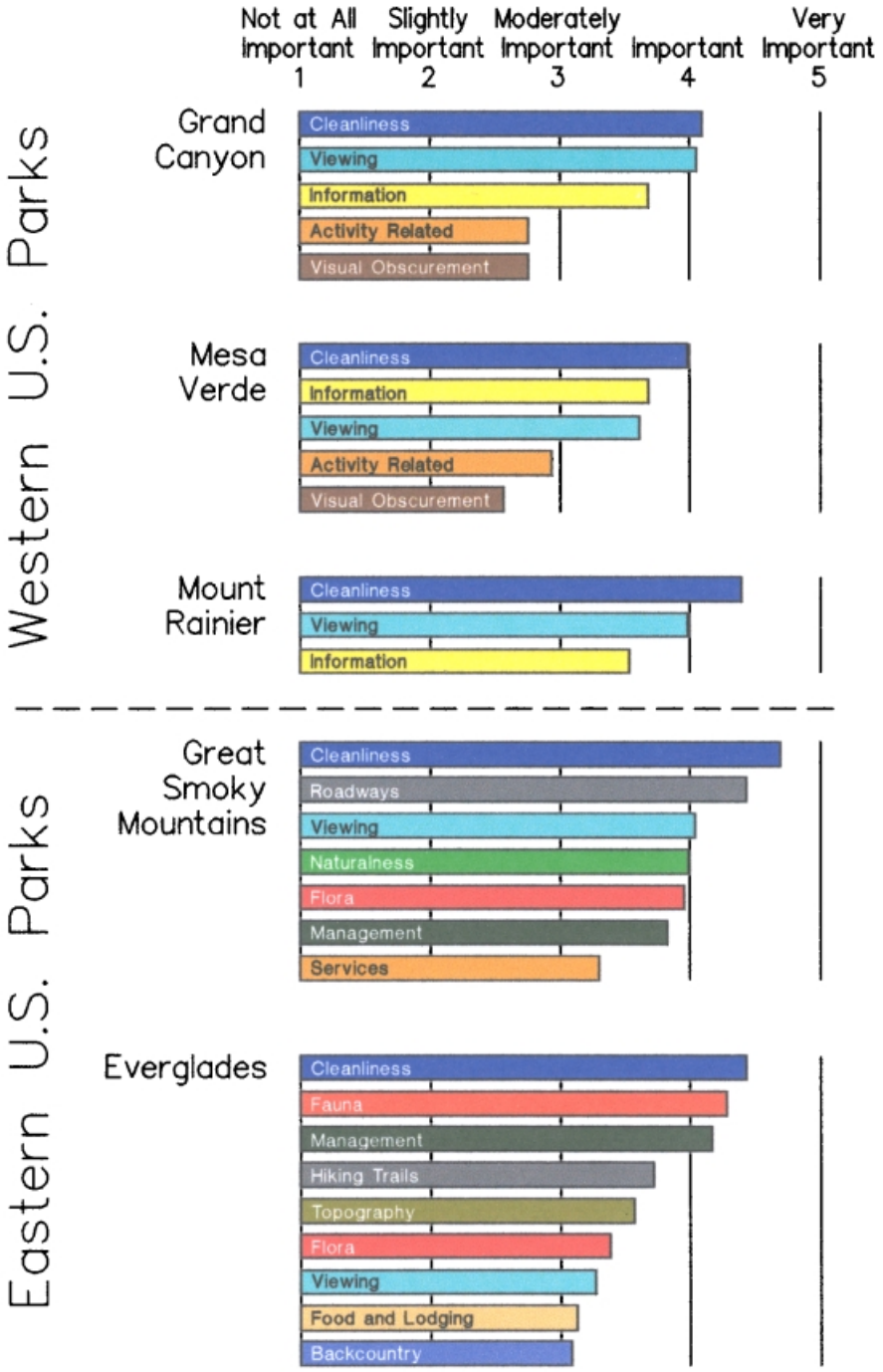

Figure 30 (Chapter 16) Relative importance of attribute clusters at five national parks.

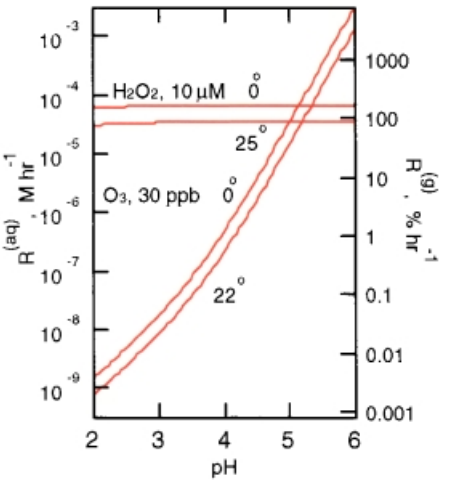

Figure 3 (Chapter 17) Instantaneous rate of aqueous-phase oxidation of S(IV) by H_2O_2 and O_3, evaluated as a function of pH for representative nonurban reagent concentrations. The rates scale approximately linearly with reagent concentrations. The right-hand ordinate gives the oxidation rate of SO_2 referred to the gas-phase partial pressure and expressed as percent per hour for a liquid water content $L = 1 \times 10^{-6}$ ($1\ cm^3/m^{-3}$), the rate scales approximately linearly with L. For the H_2O_2 reaction the indicated aqueous-phase concentration of H_2O_2 corresponds to total mixing ratio of this species (gas plus aqueous phase; the two are comparable) of $\sim 0.6 \times 10^{-9}$.

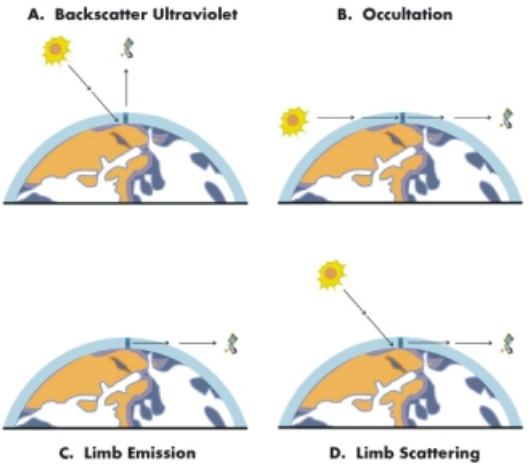

Figure 2 (Chapter 21) Schematic diagram showing the spacecraft and atmosphere geometry for the four common methods of acquiring trace gas measurements from satellite instruments.

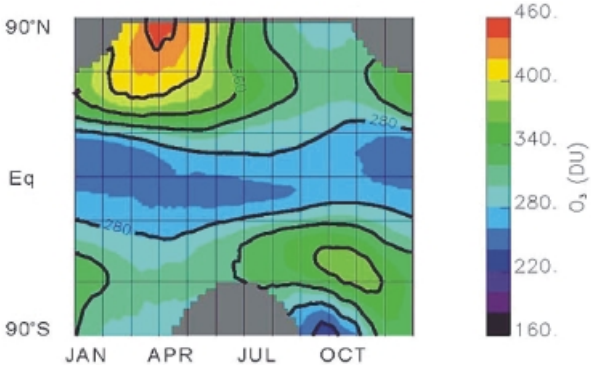

Figure 3 (Chapter 21) Two-dimensional (latitude/season) representation of total column ozone as measured by TOMS for the period 1978 to 1993.

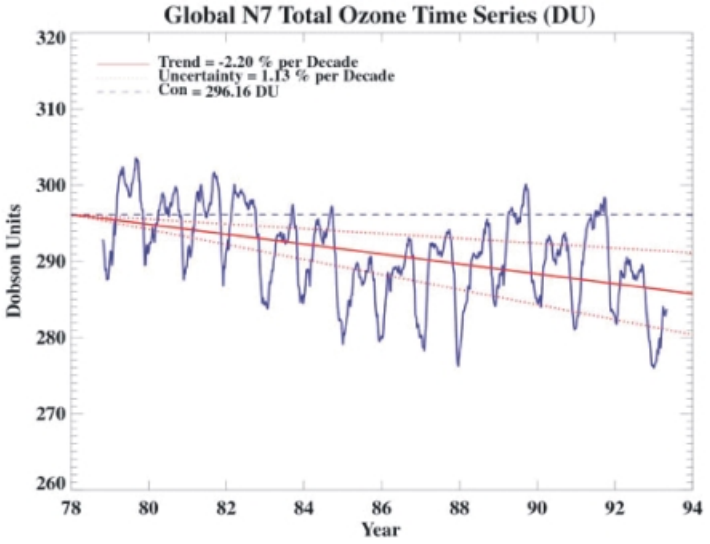

Figure 4 (Chapter 21) (*a*) Long-term trend determined from TOMS data over the period from 1978 to 1994 after correcting for seasonal cycles, the 11-year solar cycle, and the quasi-biennial oscillation.

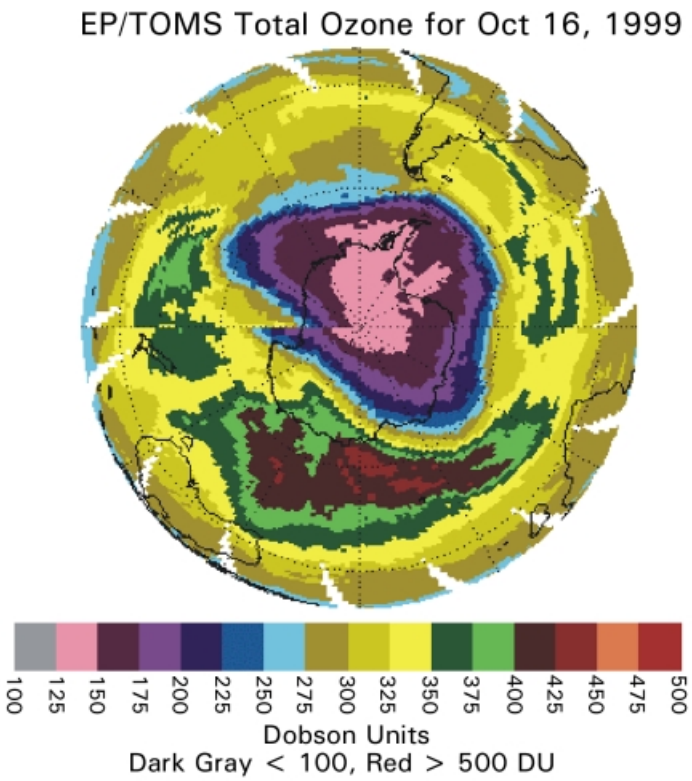

Figure 5 (Chapter 21) Map of total column ozone over the Antarctic as determined from TOMS October 16, 1999.

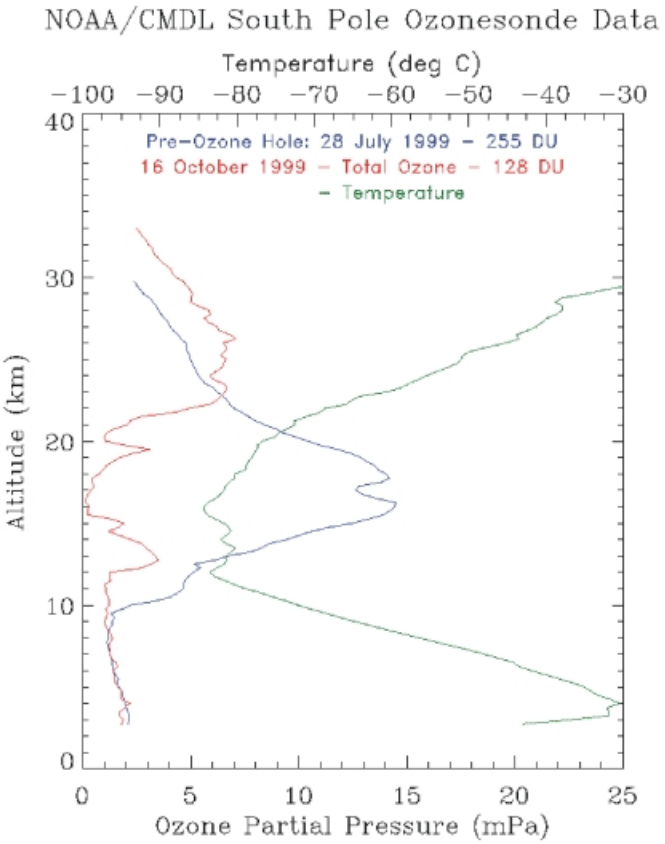

Figure 6 (Chapter 21) Plot of vertical profile of ozone (blue and red lines) over the South Pole as measured from ozonesondes during austral winter (July 28) and spring (October 16), 1999; temperature profile for October 16 is also shown (green line).

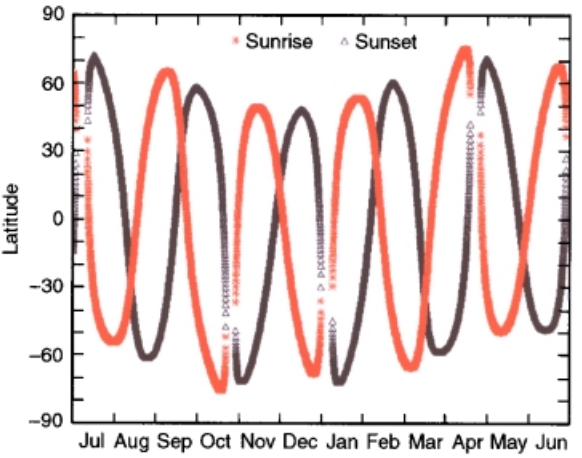

Figure 7 (Chapter 21) Spatial coverage of solar occultations from the SAGE II instrument as a function of season. Sunrise and sunset occultations are indicated with different symbols. There is excellent year-to-year repeatability of the times and locations of the occultations.

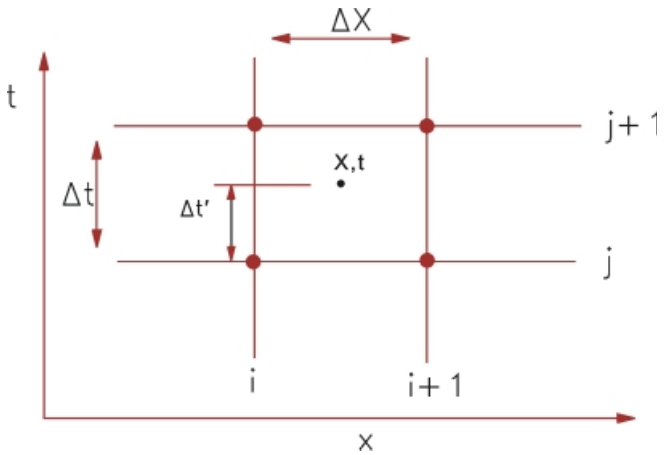

Figure 1 (Chapter 30) The *x–t* solution domain for the weighted four-point implicit scheme.

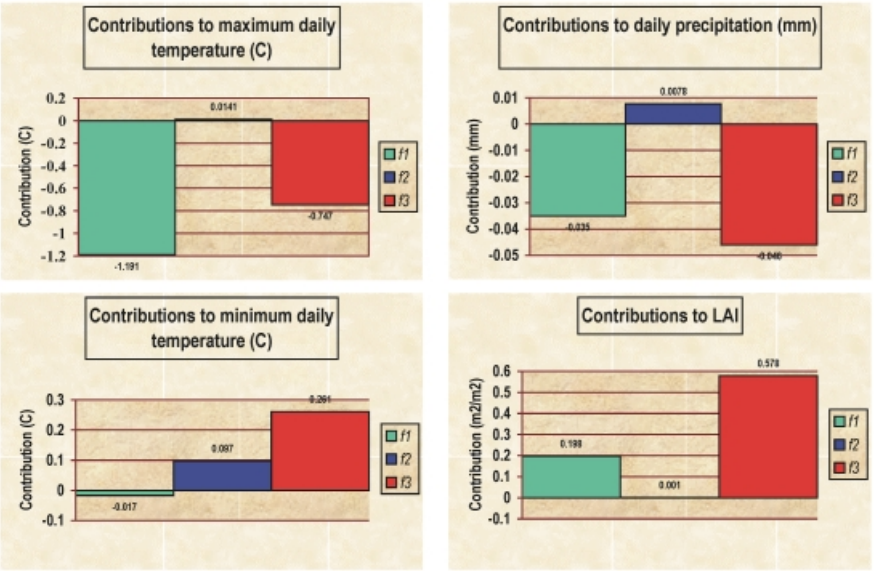

Figure 2 (Chapter 32) RAMS/GEMTM coupled model results—the seasonal domain-averaged (central Great Plains) for 210 days during the growing season, contributions to maximum daily temperature, minimum daily temperature, precipitation, and leaf area index due to f1 = natural vegetation, f2 = 2XC02 radiation, and f3 = 2xC02 biology. (*Adapted from Eastman et al., 2001*).

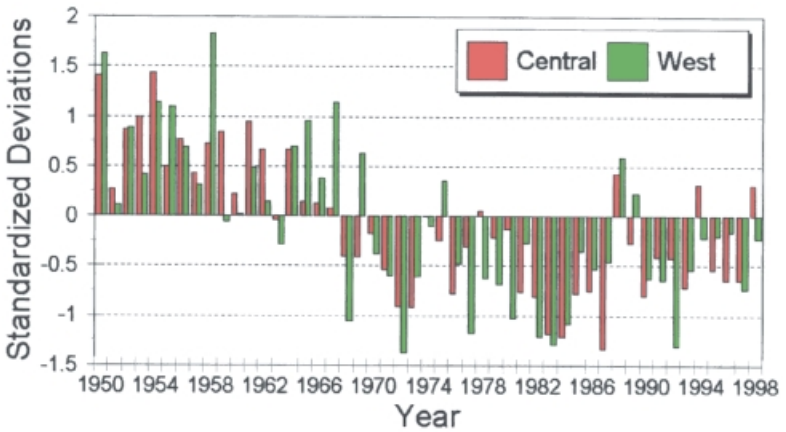

Figure 3 (Chapter 32) Swings or shifts of the time series of standardized deviations of annual rainfall for Central and West Sahel areas during the period 1950–1998. (*After Landsea et al., 1999*.)

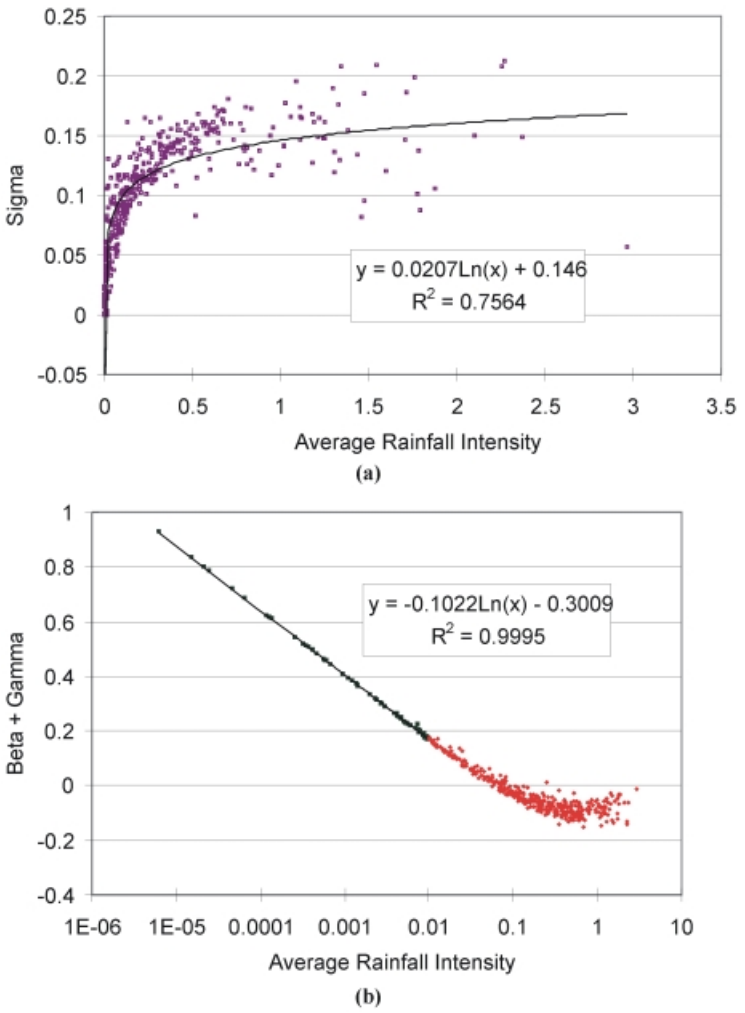

Figure 5 (Chapter 33) (*a*) Sigma vs. average rainfall intensity and (*b*) Beta + Gamma vs. average rainfall intensity (from Kang and Ramirez[46]).

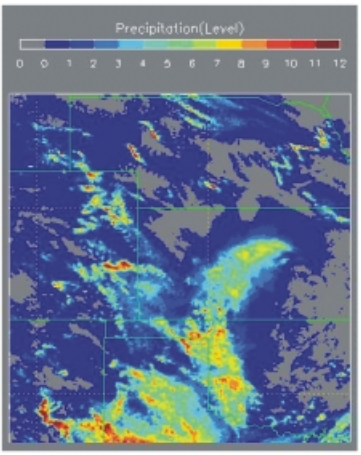

Observation

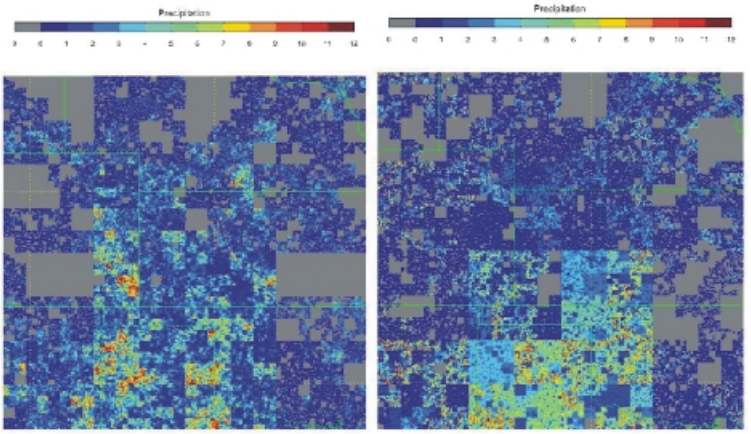

β-lognormal model

Nonparametric hierarchical model

Figure 6 (Chapter 33) Comparison of observed and downscaled rainfall fields (July 6, 1997) (from Kang and Ramirez[46]).

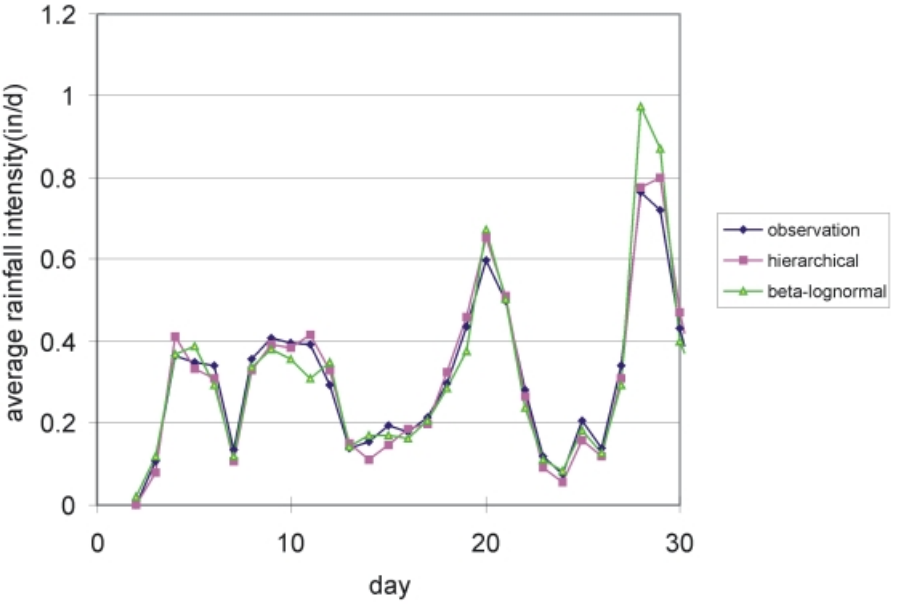

Figure 7 (Chapter 33) Time series of average rainfall intensity (NEXRAD, July 1997) (from Kang and Ramirez[46]).

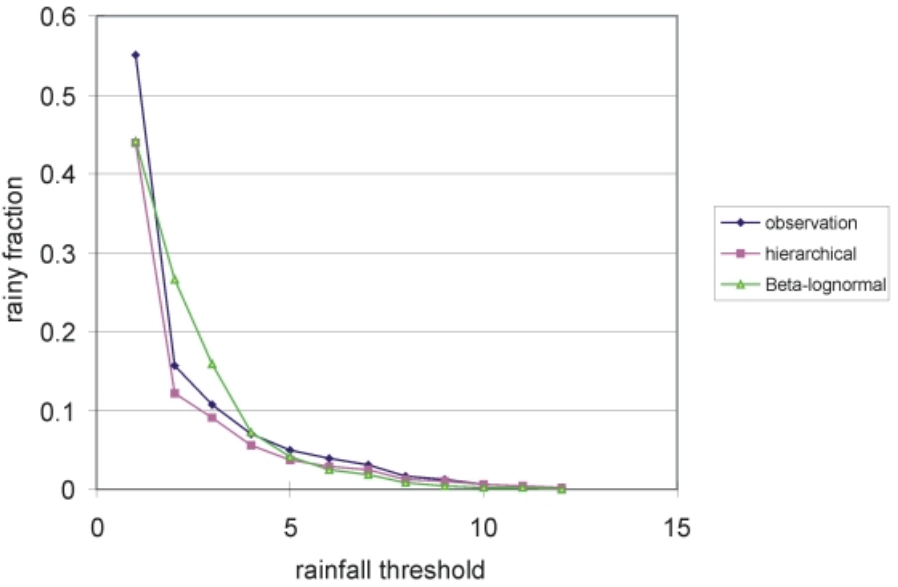

Figure 8 (Chapter 33) Rainy fraction as a function of rainfall threshold (NEXRAD, July 6, 1997) (from Kand and Ramirez[46]).

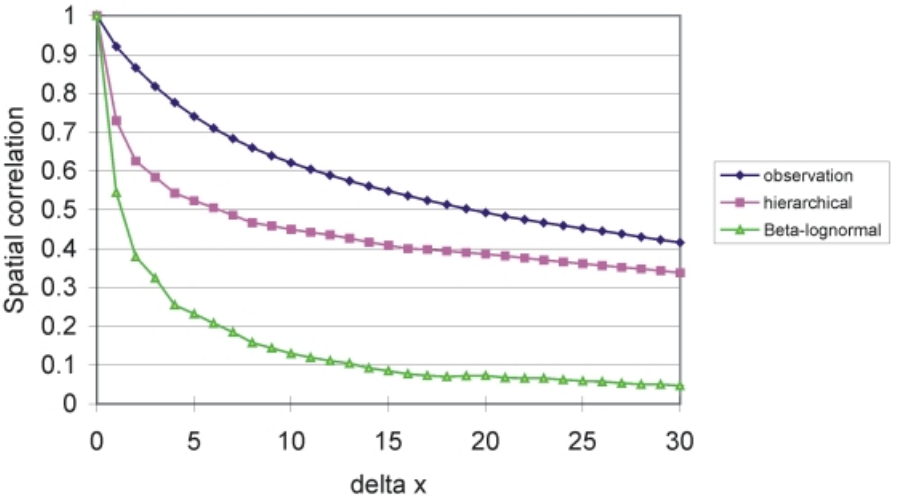

Figure 9 (Chapter 33) Comparison of correlation function for monthly rainfall (from Kang and Ramirez[46]).

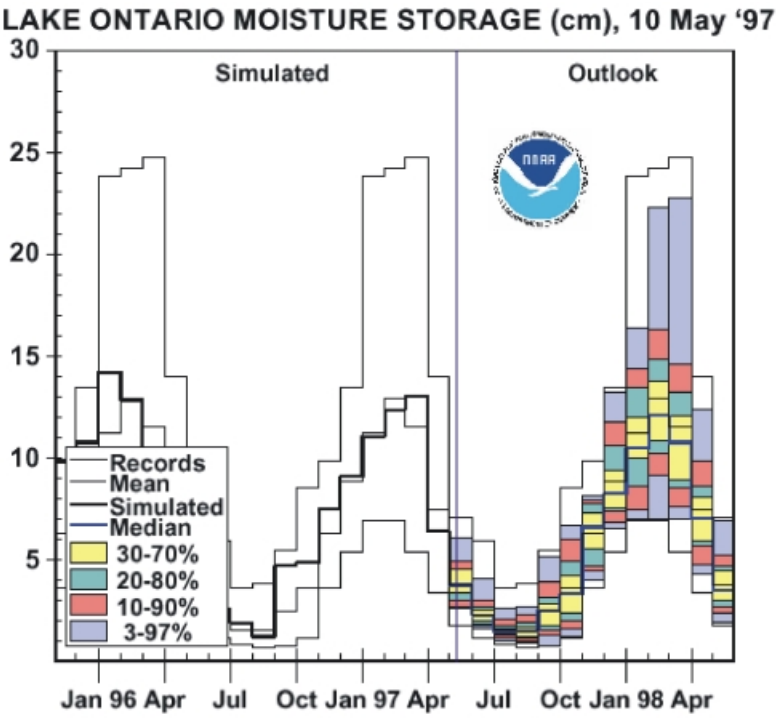

Figure 5 (Chapter 34) Example of hydrologic forecasts using climate outlooks (from Croley, 1997, 2000).

Figure 1 (Chapter 36) Quebrada San Julián upstream of Caraballeda showing evidence of recent debris flows and flash floods. Note the high slope angles, large numbers of debris flow scars, and abundance of new alluvium and colluvium in the channel bed and fan surface.

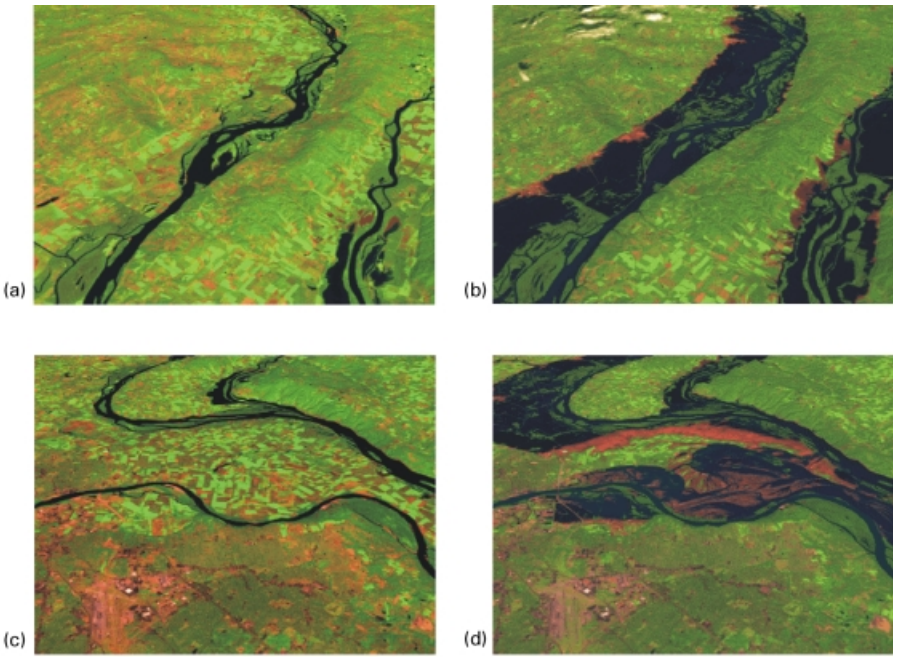

Figure 2 (Chapter 36) (4 panels) These scenes show various sections of the Mississippi River near St. Louis before and just after the 1993 floods, which peaked in late July/early August. The images show the area as seen by the LandSat Thematic Mapper (TM) instrument. The short-wave infrared (TM band 5), infrared (TM band 4), and visible green (TM band 2) channels are displayed in the images as red, green, and blue, respectively. In this combination, barren and/or recently cultivated land appears red to pink, vegetation appears green, water is dark blue, and artificial structures of concrete and asphalt appear dark gray or black. Reddish areas in the scenes during the flood show where water had started to recede, leaving barren land.

Figure 3 (Chapter 36) Water and sand washed inland to make travel difficult in North Topsail Island, North Carolina, after hurricane Fran.

Figure 4 (Chapter 36) Arizona flash flood, Wenden, Arizona. This community was flooded twice in late October 2000 when waters from Centennial Wash swept into the town. (Photo courtesy of U.S. Small Business Administration.)

Figure 5 (Chapter 36) Elevated home in West Virginia is a mitigation success story. Risk is greatly reduced to homes elevated before a flood.

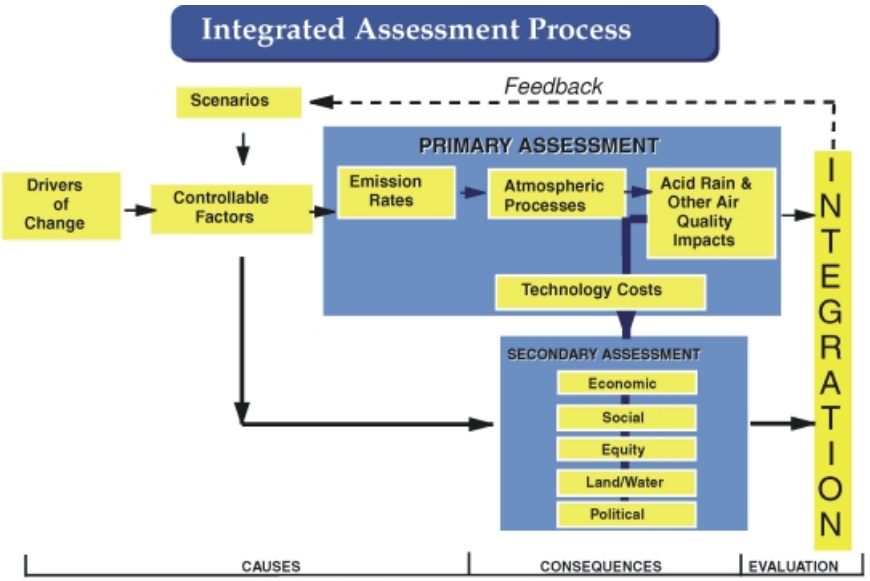

Figure 1 (Chapter 49) Important elements to consider in an assessment of acid rain in the context of other important environmental, energy, and economic concerns.